Identification of Ductile to Brittle Transition Temperature by using Plane Strain specimen in Tensile Test and Correlation with Instrumented Charpy Impact Test: Experimental and Numerical study

Frank TIOGUEM [a 1, 2], Matthieu MAZIERE [1], Franck TANKOUA [2], André GALTIER [2] and Anne-Françoise GOURGUES-LORENZON [1]

[1] MINES ParisTech, PSL Research University, MAT - Centre des matériaux, CNRS UMR 7633, BP87 91003 Evry cedex, France
[2] ASCO Industries - Centre de Recherche CREAS, BP 70045, Avenue de France, 57301 Hagondange cedex, France

Abstract

This study addresses the correlation between the ductile-to-brittle transition (DBT) temperature range of high strength 4140 steel obtained respectively from tensile tests under plane strain (PS) conditions and from conventional Charpy Impact tests. Specimens were taken respectively at 25 mm (P) and at 55 mm (M) from skin of a cylindrical 90-mm-radius hot rolled bar water quenched from 875°C, tempered at 600°C and air cooled. P and M samples respectively showed a fully martensitic and a martensite-bainite microstructure. Fracture surface observations showed good agreement for physical fracture mechanisms (cleavage facet size, mixed ductile + brittle fracture in the transition region, ductile fracture at higher temperatures) between PS and Charpy, in particular sensitivity of upper bainite to cleavage fracture that reduces fracture energy in the lower shelf-energy on Charpy tests.

Key words: Martensite-bainite / Carbides / Charpy test / Notched plane-strain specimen / Experimental and numerical study

1. Introduction

High strength, quenched and tempered steels have been largely used since decades for manufacturing of off-shore drilling parts and many components automotive gearboxes. High yield strength and good impact toughness are required as design criteria for such applications. Yet, as reviewed by e.g. Beranger et *al*. [1], improving strength of these steels generally implies decreasing their impact toughness. The mechanical properties of this steel can be tuned by improving their final heat treatment [2]. In certain cases, an increase in tempering temperature is shown to increase impact toughness in the upper self-energy (USE) range, yet at the expense of yield strength. Improving the trade-off between these two mechanical properties is therefore required to optimize in-service properties of components. The two microstructural components that have to be optimized in this way are (i) the martensitic matrix and (ii) the population of carbides that are formed during tempering.

The present study focuses on a 1%Cr-Mo AISI 4140 steel. After final normalizing, quenching and tempering, it is known to present a mixed structure of tempered martensite and lower bainite that is also

[a] Corresponding author : frank.tioguem-teagho@mines-paristech.fr

known to improve yield stress and tensile strength up to about 30% in spite of only martensite matrix. Tomita [3] shows that a previous high temperature thermomechanical treatment (HTMT) improves USE with respect to deformation-free heat treatment on 4340 steel. The improved mechanical properties are attributed to the sub-cell structure introduced in austenite by processing HTMT and inherited martensite. In a tempered martensitic steel (0.3C - 0.5Si - 2Mn – 0.001P – 0.001S), Takebayashi et *al*. [4] showed that refining microstructural parameters such as the prior austenite grain size improved the USE going up to 30J, but no significant effect of carbide size distribution was mentioned in this study. Im et *al*. [5] showed that increasing molybdenum and reducing the carbon content can improve the USE, by enhancing precipitation of M_2C-type alloy carbides instead of cementite, whose size is much lower than the critical carbide size to initiate fracture. In the Im's study, observations of polish fracture surface from tensile tests at ductile fracture region using round-notched cylindrical specimens revealed that the vicinity of M_3C are major initiated site of cracks.

Charpy impact testing is a powerful tool to study the ductile-to-brittle transition (DBT) of body-centered cubic (bcc) materials as a function of temperature but mechanical analysis of the test is difficult due to self-heating, strain rate sensitivity and contact issues. Moreover, the link between impact toughness and fracture toughness is not obvious in many cases, in particular, for bainitic and martensitic steel microstructures. The local approach to fracture has been introduced to solve this issue as reviewed by Pineau et *al*. [6]. In this approach, identification of the resistance of the material to fracture requires taking the local heterogeneity in microstructure into account. The local approach to fracture is classically based on tensile tests on notched cylindrical specimens. However, in high strength alloys reinforced by precipitation or by ductile fracture might be sensitive not only to the stress triaxiality ratio, η (of the hydrostatic stress to the Von Mises equivalent stress) but also to the third invariant of the stress tensor, as commonly represented by the Lode angle, θ [7] in fact, Changing the geometry of specimens from round notched bars ($\cos(3\theta) = 1$) to plane strain specimens ($\cos(3\theta) = 0$) [8] can lead to applying a stress state closer to that experienced in Charpy three-point-bending specimens, both in terms of triaxiality and Lode parameter. To this aim, a new experimental approach making use of double side notched plane strain specimen is proposed in this study. The numerical analysis of tests on these specimens is expected to be much easier than that of Charpy tests.

The purpose of the present study is to investigate correlations between the DBT behavior of a high strength 4140 steel obtained respectively from tensile tests under plane strain conditions and from conventional Charpy impact tests. The effect of microstructure (both of matrix and carbides) on the ductile fracture behavior in the USE domain, the fracture mechanisms and the state stress are also addressed.

2. Experimental procedures

2.1. Material and metallographic procedures

The chemical composition of the steel is given in Table 1. Two samples of the same cylindrical bar were taken respectively at 25 mm (P) and at 55 mm (M) from the skin of a cylindrical 90 mm radius hot rolled bar water quenched from 875°C, tempered at 600°C and air cooled. P and M microstructures respectively showed fully martensitic and a martensite-bainite matrix, with two types of carbide particles. The average Vickers micro-hardness (weight 300g, dwell time 10s) of the two microstructures was $HV_{0.3} = 344 \pm 15$ for microstructure P and $HV_{0.3}=316 \pm 30$ for microstructure M.

Table 1: Chemical composition of AISI 4140 steel (wt. %)

C	Mn	Si	Ni	Mo	Cu	P	S	Al
0.401	1.143	0.274	0.20	0.32	0.11	0.011	0.005	0.018

For metallographic analysis, samples were polished to final 1µm diamond paste then etched in a 4% nital solution. In order to investigate the size distribution of carbides in detail, the plane perpendicular to the bar axis was chosen. Carbon extractive replicas was prepared by the same polishing and etching procedure, then coating the sample surface with a 50-nm-thick carbon film by using a QUORUM Q150T evaporator. The film was released from the sample by immersion in a 10% nital solution. The expected nature of carbides in such Cr-Mo quenched + tempered steels is composed of larger, rod-like or spherical M_3C together with smaller, needle-like M_2C[5].

Microstructural observations, including carbide distribution on extracted replicas and fracture surface observations were conducted using a Sigma300 and a FEI Nova NanoSEM 450 field-emission gun SEMs. From scanning electron microscope (SEM) images of the replicas, distributions of particle size and of the nearest-neighbor distance between carbides were estimated. Carbide size distributions were determined using common thresholding procedures of the ImageJ® software. Two parameters were considered during particle analysis for discrimination, the size and the cylindricity. The nearest-neighbor distance between carbides were calculated by the SKIZ geodesic method which is based on mathematical morphology considerations, with Matlab® software; this method takes the shape and the border of each particles (and not only the center of mass) into account. Several thousands of particles were analyzed for each microstructure. For M_2C carbides, about 10 manual measurements were made on a limited number of carbides for estimation of the average width, *w*. The size of M_2C carbides was then determined as their so-called equivalent length, i.e., the length of a rectangular particle having a fixed width equal to *w* and the same area as the measured carbide.

2.2. Mechanical tests

To characterize the DBT behavior of both microstructures, instrumented Charpy impact tests (ICITs) were performed first using 2 mm-deep V-notched specimens ($10 \times 10 \times 55$ mm^3). Three specimens were broken at each test temperature ranging from -60°C to +60°C. An instrumented impact pendulum device, with a nominal impact velocity of 5 $m.s^{-1}$ was used.

Two kinds of quasistatic tensile tests were performed along longitudinal direction of the bar by using a 250 kN servohydraulic Instron8500 machine. First, tests at room temperature were performed at prescribed elongation rate of 10^{-3} s^{-1} on smooth cylindrical (SC, Fig 1a) and smooth plane strain (SPS, Fig. 1b) specimens. To identify the DBT behavior in plain strain conditions by the local approach of fracture, tensile tests were performed on double-side notched plane-strain (NPS) specimens (Fig. 1c) in a climatic chamber at -60°C, -20°C, +20, +60°C. The specimen temperature was controlled to ± 1°C by using a thermocouple spot welded on the specimen end.

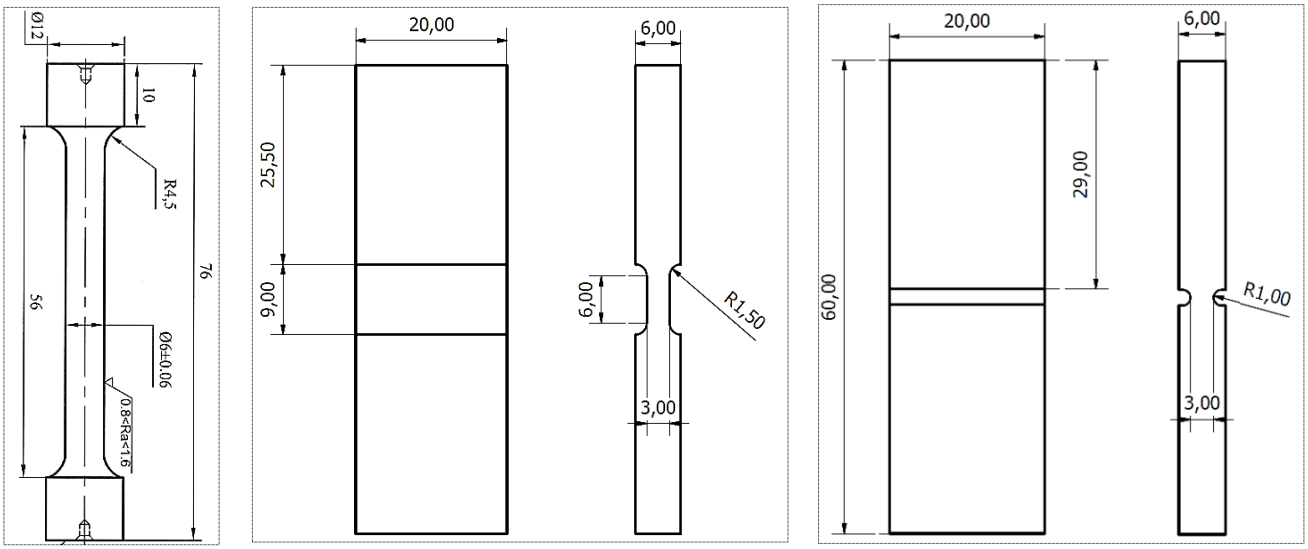

(a) (b) (c)

Fig. 1: Dimensions (in mm) of (a) SC. (b) SPS and (c) NPS specimens.

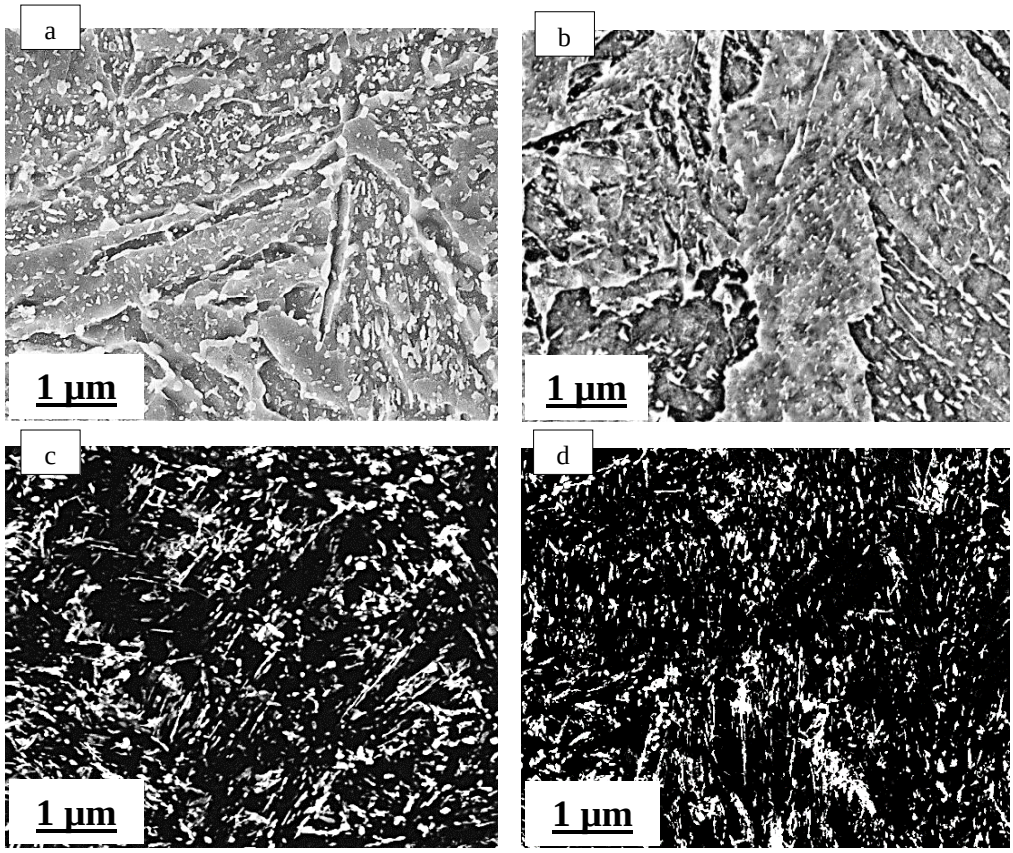

Fig. 2: Typical SEM images of etched samples of (a) P and (b) M microstructures. Typical SEM images of extractive replicas of (c) P and (d) M microstructures.

3. Results

3.1. Microstructure and carbide distributions

As shown in Fig. 2, P and M microstructures show martensite laths and mixed martensite and bainite, respectively. Assuming the tempering temperature (600°C), it seems to be upper bainite. Several types of carbide were identified within the matrix. Detailed analysis of carbon replicas showed two types of carbides, namely, (i) larger, elongated rod-like and spherical particles that could be M_3C carbides and (ii) much finer, needle-like carbides, probably of the M_2C type. M_2C also tends to be dispersed in the martensite matrix but, in the present case, the spatial distribution of M_2C appeared very heterogeneous.

The results of statistical analysis on extracted replicas images are presented in Fig. 3. About 2000 particles were analyzed for the size distribution of M_3C and M_2C carbides, 15000 nearest-neighbor distances between M_3C carbides and 20000 nearest-neighbor distances between M_2C carbides for each of the P and M microstructures. SKIZ method allows the determination of nearest-neighbor distances between only (e.g) M_3C carbides while taking into account the influence area of M_2C carbides. Thus to avoid sur-estimation of the distances obtained. For both microstructures, the average width *w* of M_2C carbides is 0.035 µm . All the results are presented in the table 2.

Except for some coarser M_3C particles found in the P microstructure, the carbide size distribution were rather similar in the two microstructures, M_3C carbides being slightly coarser and M_2C slightly smaller for the P microstructure. The distance between M_3C carbides did not strongly depend on microstructure, whereas that between M_2C carbides was slightly larger for the M microstructure.

Table 2: Result of carbide size and nearest-neighbor distribution distance analysis.

Specimens	M_3C (mean diameter, µm)	M_3C (mean nearest-neighbor distance, µm)	M_2C (mean length, µm)	M_2C (mean nearest-neighbor distance, µm)
P	0.20	0.15	0.053	0.14
M	0.17	0.20	0.053	0.17

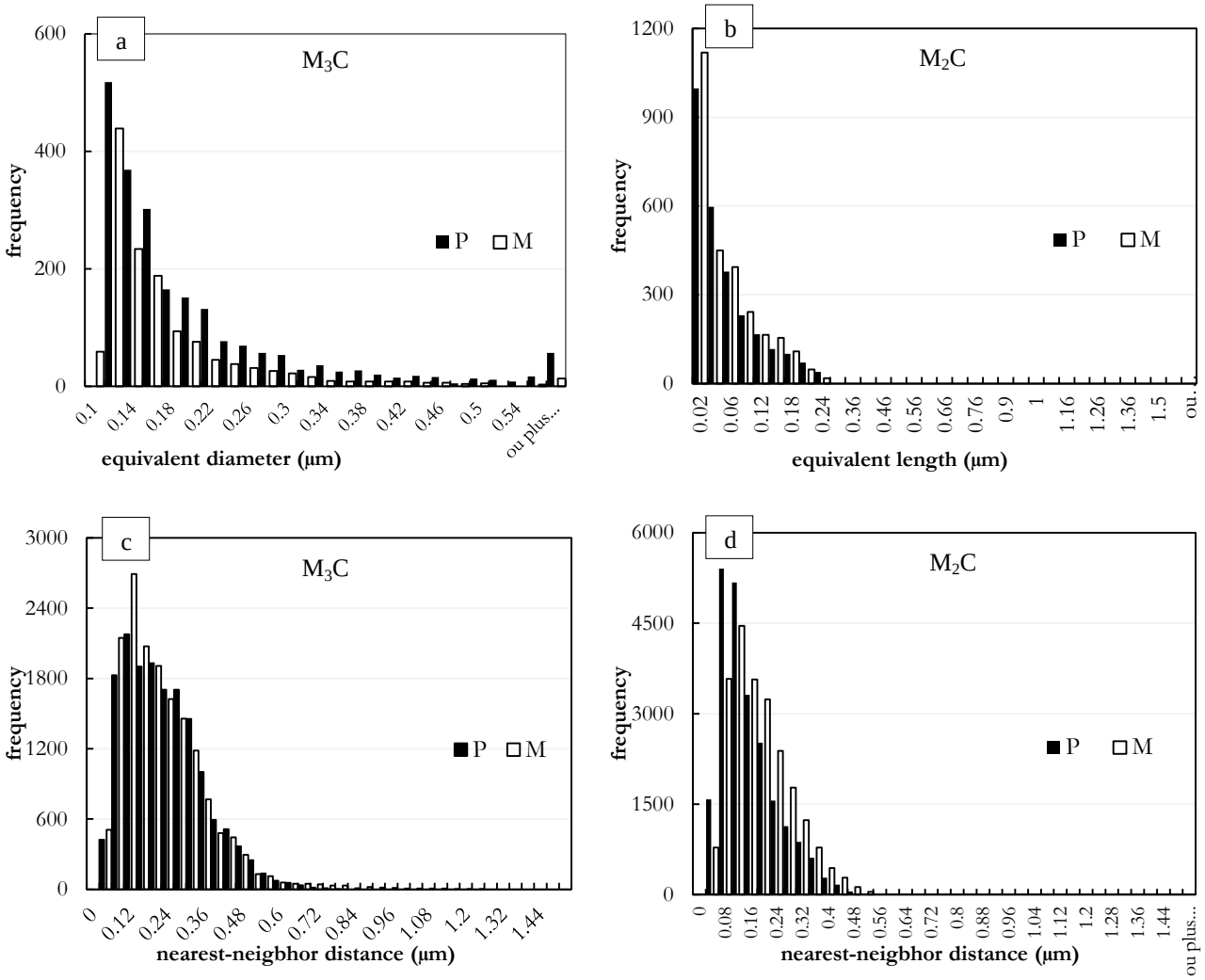

Fig. 3: (a) and (b) carbide size distribution. (c) and (d) distribution of nearest-neighbor distances between M_3C and M_2C carbides, respectively.

3.2. Tensile properties of smooth specimens

Fig. 4 shows the load-displacement curves of P and M microstructures at room temperature. Based on conventional tensile tests on SC specimens (Fig. 4a), the general tensile properties of materials are respectively for P and M microstructures: yield strength 900 and 720 MPa, tensile strength 1050 and 950 MPa, maximum uniform elongation 0.058 for both, fracture elongation close to 0.16 for both. Thus, microstructure P was stronger than microstructure M, but they displayed similar ductility. Tensile tests on SPS specimens, Fig. 4b were performed to facilitate identification of constitutive parameters. Plane strain tensile results confirmed that microstructure P was stronger than microstructure M. Anyway, there was a slight difference in maximum uniform axial elongation in SPS specimens between the two microstructures (4.3% at 1130MPa for microstructure P and 4% at 1000MPa for microstructure M).

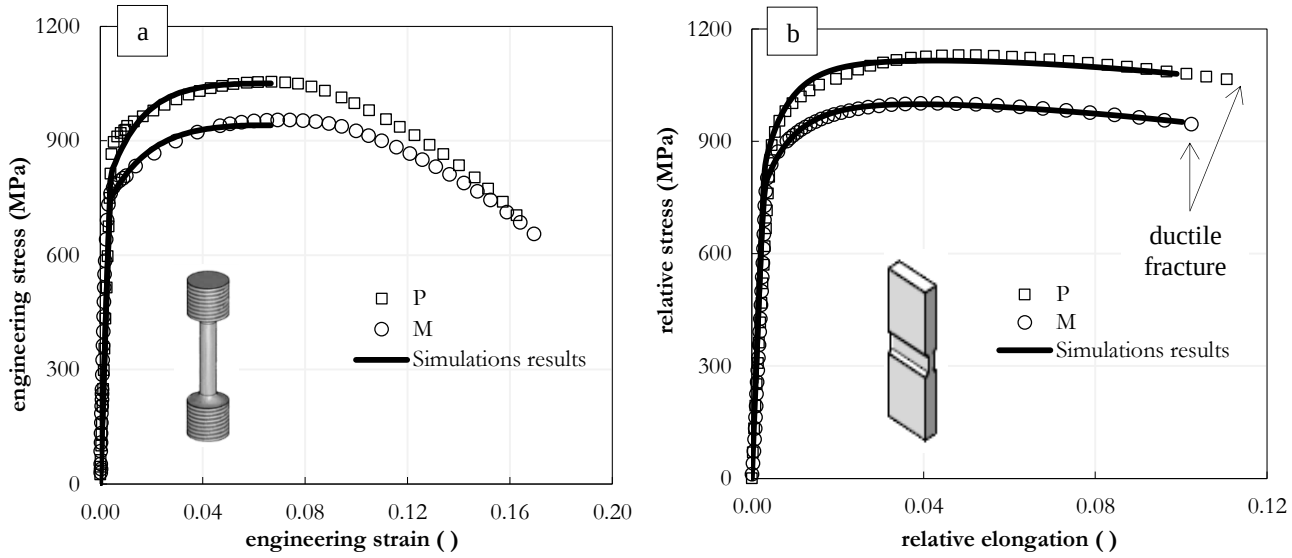

Fig. 4: Axial stress vs. axial elongation curves for tensile tests on: (a) SC and (b) SPS specimens. Symbols: experiments; lines: model predictions.

3.3. Charpy impact properties

3.3.1. General behavior and associated fracture mechanisms

Typical load vs. hammer displacement curves from ICIT tests are reported in Fig. 5. These curves were divided into two parts [10]. In the first part, the load increases up to the maximum value, F_{max}, this point being attributed to fracture initiation. In the second part of the curve, the load decreases steadily or abruptly up to the end of the test, due to crack propagation and final fracture. As reviewed in [4], the shape of this curve strongly depends on the test temperature. Abrupt load drops are attributed to brittle, unstable crack propagation, whereas ductile fracture generally induces a stable decrease in the load vs. displacement curve. This was actually the case for the considered steel; Charpy specimens associated to significant load drops in the curve exhibited a significant area fraction of flat brittle fracture (see general views of Fig. 5). Screenivasan et *al* [11] investigated martensitic stainless steel and categorized the ICIT waveform of a martensitic stainless steel into 3 types: type I, II and III, which correspond to brittle, mixed (brittle + ductile) and fully ductile fracture, respectively. The fracture surfaces, illustrated in Figs 5a and 5b for specimens broken at -60°C, -20°C and +20°C, clearly agreed with this interpretation. The DBT curves of P and M microstructures, both in absorbed energy and area fraction of ductile fracture, are reported in Fig. 6.

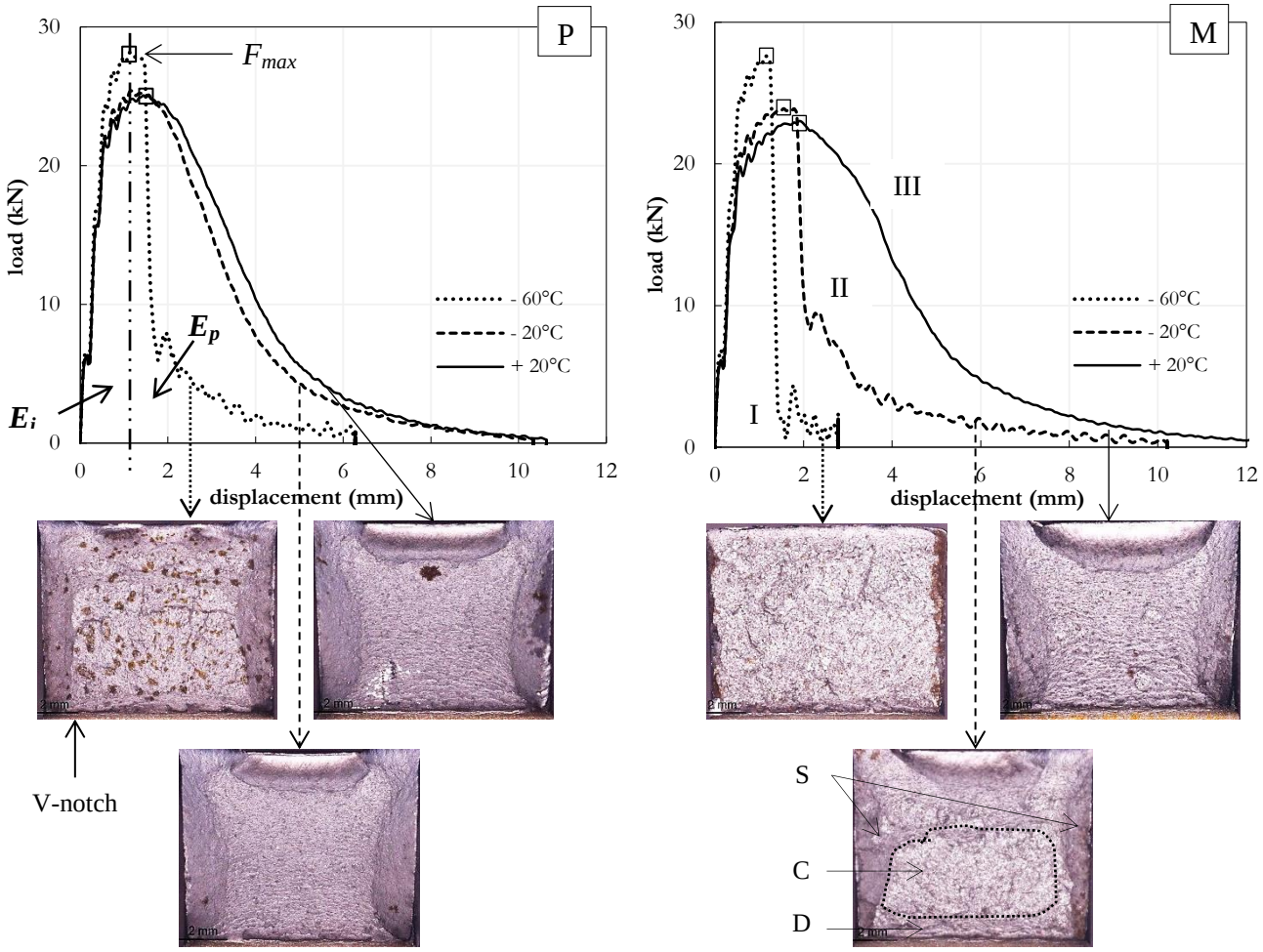

Fig. 5: Typical ICIT curves of (a) P and (b) M microstructures, together with global view of fractured specimens. The crack propagated from the bottom to the top of the images. D: flat ductile, C: cleavage, S: slant fracture.

For both P and M microstructures, the load vs. displacement curves obtained at -60°C corresponded to type I. Fracture surface were globally brittle, although there were also many ductile regions close to the sides of the fractured specimens. Type II curves were obtained at -20°C; yet, the waveform of steel M at this test temperature presented a larger load drop than that of microstructure P. On the corresponding fracture surface, the larger load drop was correlated to the presence of a wider brittle region than on the fracture surface of microstructure P at the same test temperature. Specimens corresponding to type III curves underwent fully ductile fracture, and were mainly obtained at room temperature. Moreover, for all these ductile specimens, a macroscopic wave-like shape of the fracture surface was noticed, from the notch tip up to the opposite side of the specimen. This could possibly be associated to strong strain localization in the plastic zones of the propagating crack but this point needs to be investigated in more detail before drawing any further conclusion.

Fig. 6 illustrates the corresponding fracture mechanisms at the micrometer scale. After fracture at -60°C (Figs 6a, 6b), cleavage facets connected by tearing ridges were found together with many secondary cracks. Haušild et *al* [12] explained that secondary cracks were created after the passage of

the main crack and cut the river ridges on the main crack. Increasing the test temperature up to -20°C increases the fraction of tearing ligaments (Figs 6c, 6d). At room temperature, ductile fracture occurred with about 90% area fraction of fine dimples (~ 0.3 µm) than of coarser dimples (~ 1 µm). MnS particles were found in the coarser dimples; this was confirmed using cross-section observations. Rod-like particles were observed in the fine dimples. Their size and morphology, compared with the distributions of carbides determined from extractive replicas, suggested that fine dimples actually nucleated from M_3C carbides. In fact, the effect of finer, needle-like M_2C carbides on void development could be neglected. Due to their small size (~200 nm), EDS analysis was not made for further identification of the nature of these particles on the fracture surfaces.

3.3.2. Fracture initiation and fracture propagation energy

The impact energy deduced from ICITs was obtained by calculation of the area under the load vs. displacement curves and corresponded to the total fracture energy. As shown in Fig. 7, both P and M microstructures tended to have the same transition temperature of about -20°C. As mentioned by e.g. Haušild et *al* [12], experimental data in the transition region generally show scatter. Microstructure M showed a higher upper shelf energy (116 J) than microstructure P (100 J). On the contrary, the fracture energy in the lower temperature range was about 38 J and 50 J for M and P specimens respectively. Nevertheless, the lower shelf energy did not seem to have been reached for the tested temperatures.

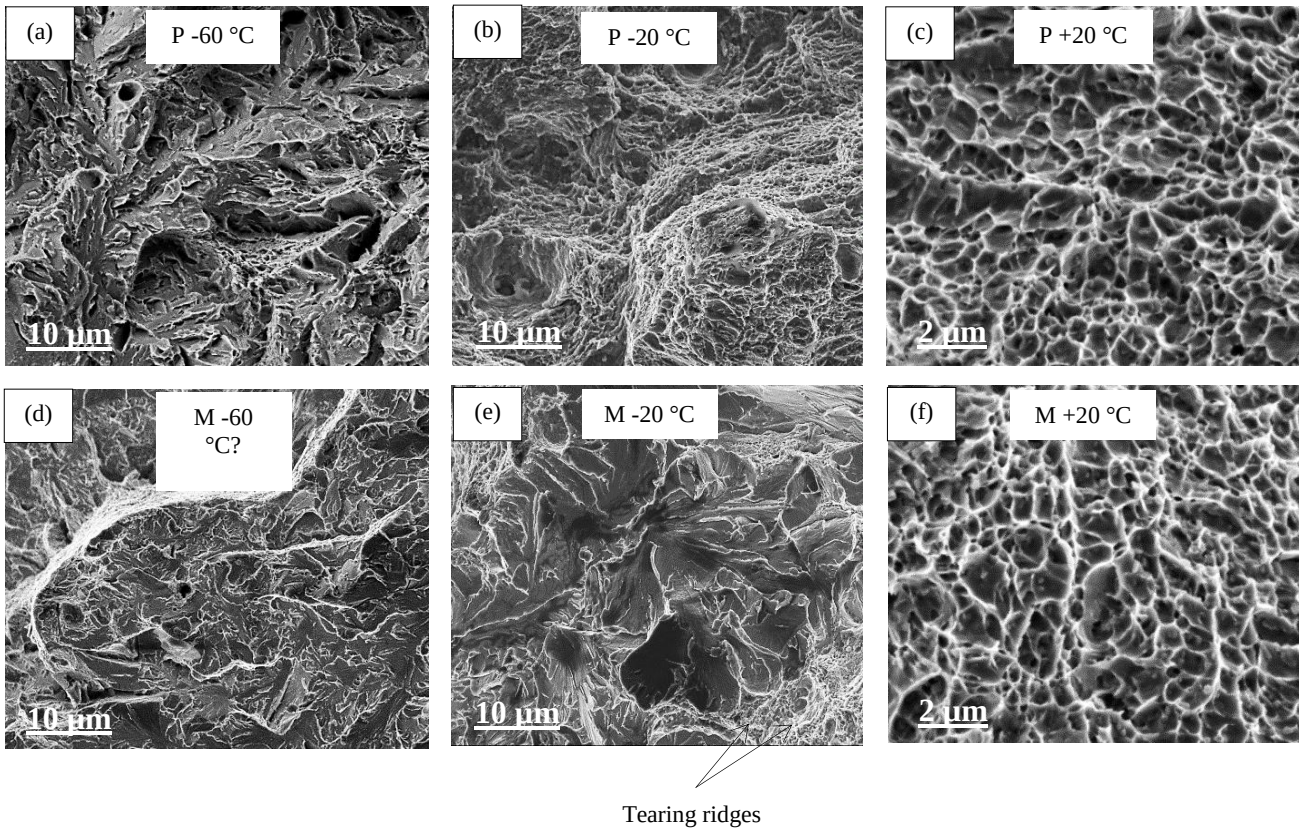

Fig. 6: Fracture mechanisms of (a,c,e) P and (b,d,f) M Charpy specimens tested at -60°C, -20°C and at room temperature.

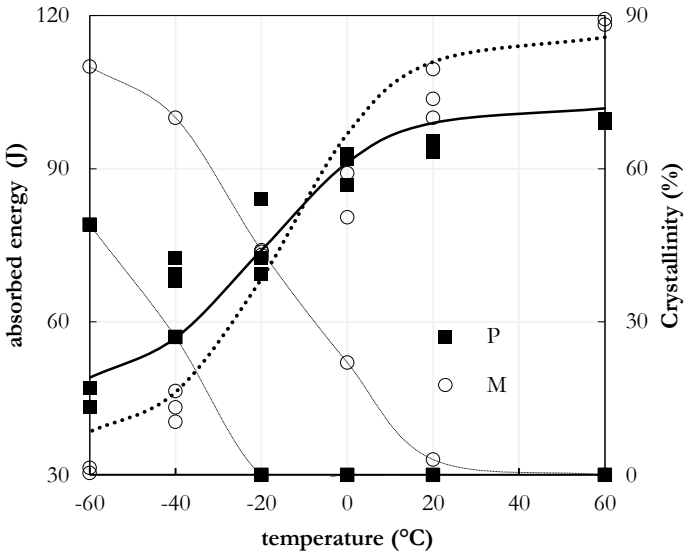

Fig. 7: Charpy impact properties of the tested steels and crystallinity.

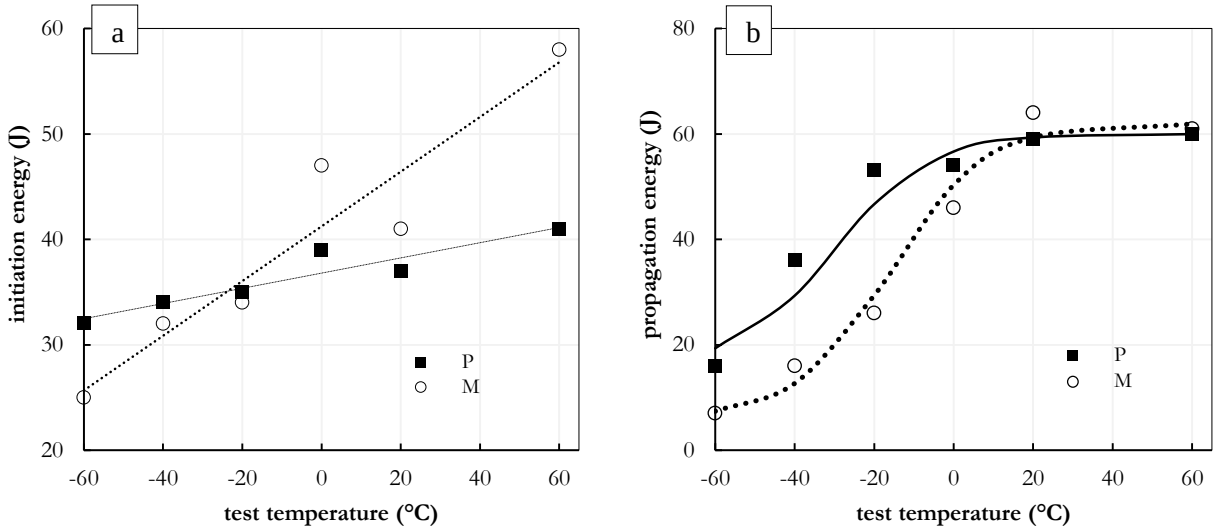

Fig. 8: Fracture initiation energy (a) and fracture propagation energy (b), plotted against test temperature.

Following the analysis of fracture energy in terms of initiation and propagation parts for martensitic steels proposed by Takebayashi et *al* [4], the energy absorbed during initiation and propagation stages are plotted against test temperature in Figs 8a and 8b, respectively. The main tendencies were as follows: (i) the fracture initiation energy depended on temperature over the whole tested range, this dependency being stronger for steel M than for steel P; (ii) this dependency was approximately linear, without any abrupt transition; (iii) for both microstructures, the change in fracture mechanism from brittle to ductile was correlated to a transition in propagation energy. Fig. 9 illustrates this result with load vs. displacement curves of specimens tested at +60°C, i.e., in the fully ductile domain. The main difference between the two specimens was on the yielding behavior and amount of strain before crack propagation.

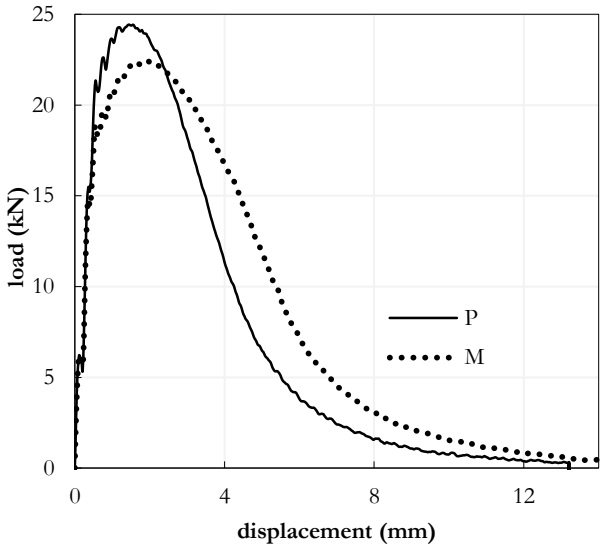

Fig. 9: ICIT waveforms of specimens tested at +60°C.

3.4. Ductile-to-brittle transition behavior investigated by the local approach to fracture

3.4.1. Experimental results

Load vs notch opening curves of tests on NPS specimens are plotted in Fig. 10. They confirmed that microstructure P was stronger than microstructure M at every test temperature. As already well-known for steels having a bcc crystal structure, increasing strength and reduction of notch opening with decreasing the test temperature were noticed for the two steels, this phenomenon being clearer for microstructure P. At -60°C, the load drop suddenly occurred after 0.2mm of notch opening for steel P . For temperatures higher than -60°C, fracture occurred once the maximum load had been reached.

Fracture surfaces are illustrated in Fig. 11. At -60°C, fracture was globally brittle. They are identified by bright facets. Salemi et *al* [13] attribute bright facets on broken surface at the effect of inter phase boundaries on the cleavage fracture. There were also some apparently planar, but rather rough cracks facets at lower temperature, resembling local intergranular cracking. NPS specimens tended to reveal them more frequently than Charpy specimens. One of these facets is surrounded in Fig. 11 (microstructure P at -60°C) by a dotted white line. It is known [2] that intergranular cracks can be sometimes attributed to reverse temper embrittlement (TE) between 450 and 600°C and linked to segregation of impurities during tempering (P, Sn, As, Sb) at grain boundaries during tempering. Nevertheless, the tempering temperatures used in the present study were higher. In the ductile regions, large and fine dimples were initiated respectively from MnS particles and M_3C carbides, as in Charpy specimens. Up to rather high temperatures (about +40°C), fracture surfaces of microstructure M showed many coarse cleavage facets corresponding to upper bainite; in fact, cleavage facets of martensite, which dominated the lower temperature fracture surfaces (see fractographs at -60°C) appeared much finer due to the intricate microtexture of martensite variants.

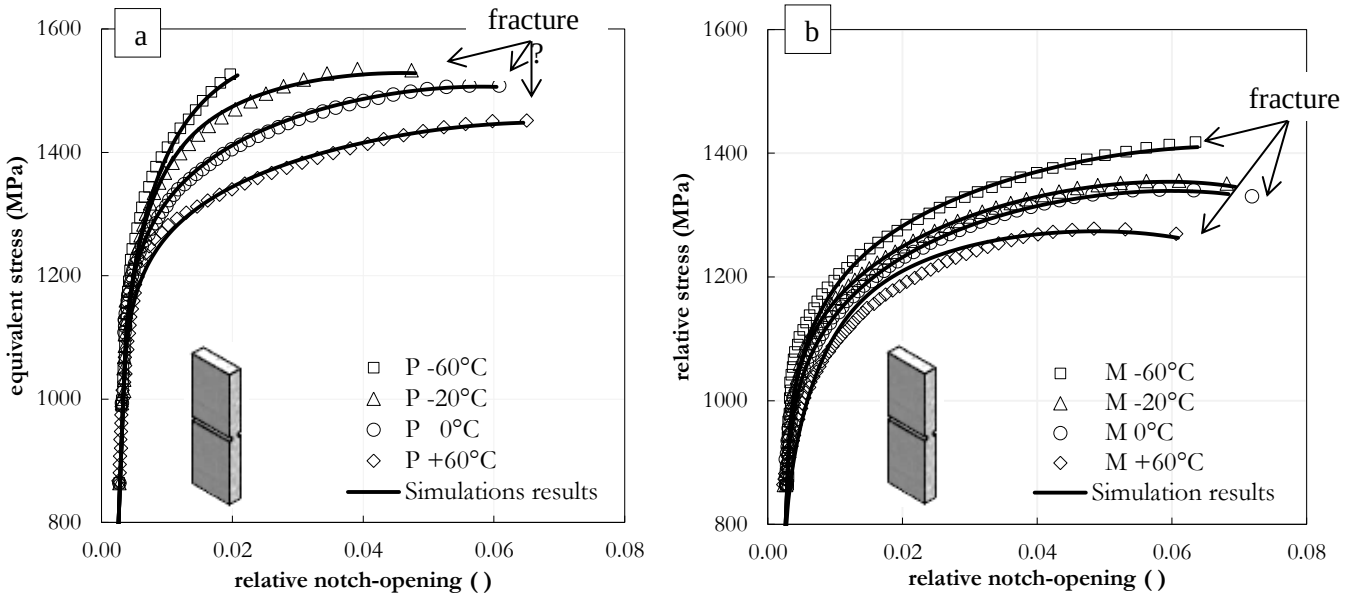

Fig. 10: Results of tensile tests at different temperatures on NPS specimens of (a) microstructure P (b) microstructure M.

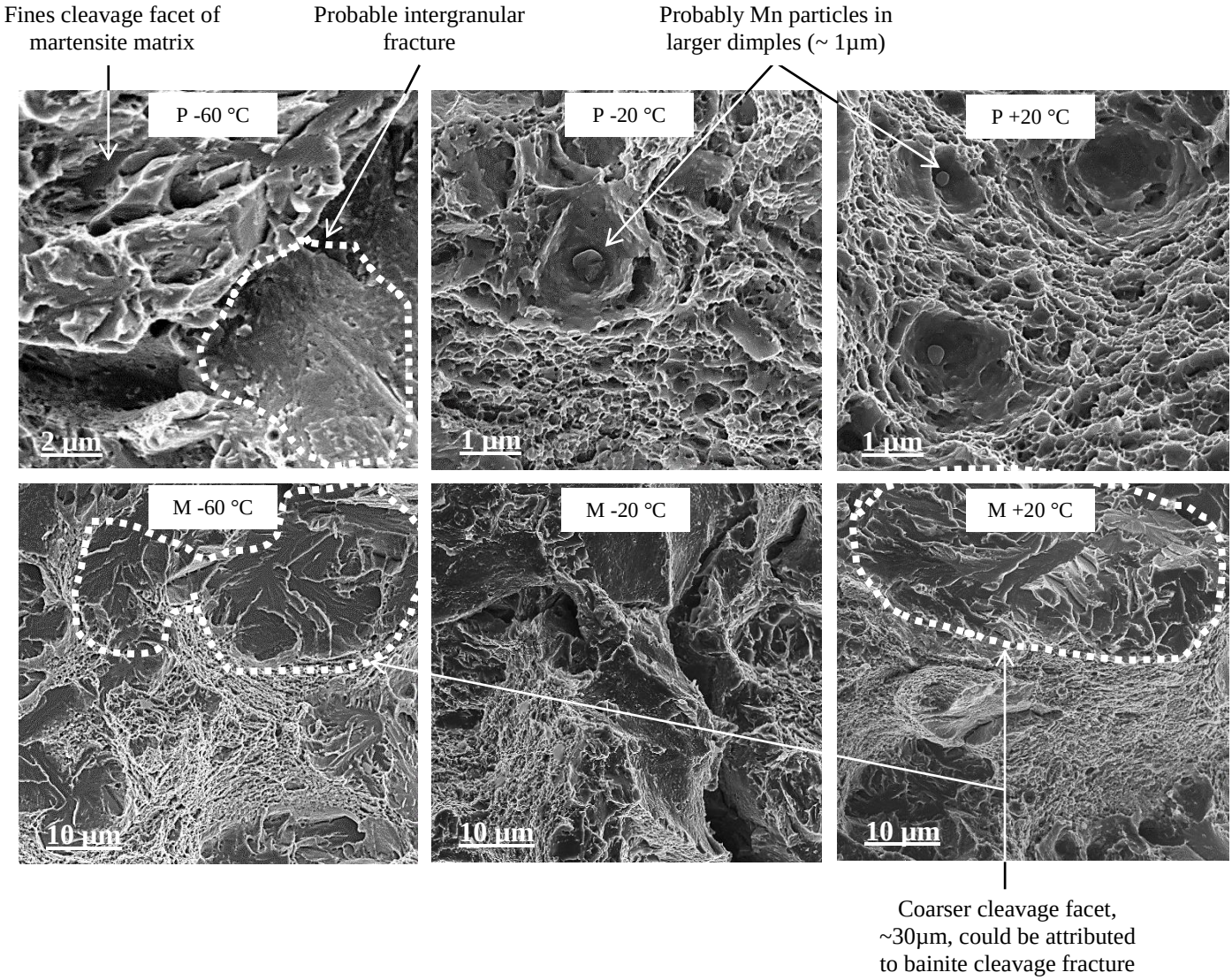

Fig. 11: Fracture surfaces of the double-side notched plane strain specimens tested in tensile at -60°C, -20°C and at room temperature.

3.4.2. Mechanical analysis

Identification and optimization of constitutive equations of the two steels were performed on Zset® in-house finite element software. First, a coupled-optimization was made based on the experimental results obtained on SC and SPS specimens. For uniaxial tension of SC specimens, only the part of the curve before necking was considered. The entire load-displacement curve for SPS specimens was simulated. Subsequently, optimized parameters were used for the numerical calculation of tests on SPS specimens.

The plastic flow behavior of the two microstructures could be well described by a Hosford yield locus, f (Eq. 1), the usual normality rule for plastic strain together with nonlinear isotropic hardening (Eq. 2), the loading path being approximately radial in the stress space:

$$f(\boldsymbol{\sigma}, p) = \sigma_H - R(p) \quad \text{with } \sigma_H = \sqrt[n]{\frac{(\sigma_1-\sigma_2)^n + (\sigma_2-\sigma_3)^n + (\sigma_1-\sigma_3)^n}{2}} \tag{1}$$

$$R(p) = R_o + \sum_i Q_i\,(1 - e^{-b_i p}),\ i = 1,2,3 \tag{2}$$

In Eq. (1), $\sigma_1 > \sigma_2 > \sigma_3$ are the eigenvalues of the usual deviator part of the stress tensor, $\boldsymbol{\sigma}$. In Eqs (1-2), Q_i, n and b_i are material parameters. R_o is the initial yield strength. In the optimization procedure, the Young modulus and Poisson's ratio were set to 200 GPa and 0.3, respectively, for both microstructures. To guide the optimization of material parameters, the maximum uniform elongation for SC tests was forced to fit with experimental data through an additional relationship between material parameters. To this aim, the Considère criterion (Eq. 3) was applied as follows:

$$\frac{dR}{dp} = R \text{ at the onset of load decrease,} \tag{3}$$

$$\text{from which one obtains } R_o - \sum_i Q_i\,[(1 + b_i)e^{-b_i p_{crit}} - 1] = 0\ ,\ i = 1,2,3 \tag{4}$$

where $p_{crit} \sim 0.058$

Optimized parameters for the behavior of tensile test on PS specimens at room temperature are presented in Table 2. From Fig. 4, good agreement with experimental results was obtained.

Table 2: Optimized parameters of the constitutive equations

Hardening rule	parameters								
	specimens	n	Ro (MPa)	Q_1 (MPa)	b_1	Q_2 (MPa)	b_2	Q_3 (MPa)	b_3
	P	7	874	241	81	312	4	106	0.1
	M	7	800	216	62	214	4	102	0.1

4. Discussion: comparison between fracture behavior in Charpy tests and in quasistatic tests on notched plane strain specimens

4.1. Fracture mechanisms

Impact toughness results showed that in the USE range, microstructure M is tougher than microstructure P. On the one hand, only M_3C carbides were observed in the fine dimples. On the other hand, the nearest-neighbor distance between M_3C carbides is nearly the same for microstructures P and M. So the only difference was on the average size of these carbides. The lower USE of microstructure P could be due to the fact that carbides were by 0.03µm larger than those of microstructure M, ductile crack initiation being possibly easier than on microstructure M. Nevertheless, the only effect of carbides could probably not explain the difference in USE. The higher impact toughness of microstructure M in the USE range could also be attributed to bainite. The lower strength of bainite-containing microstructure M was probably overwhelmed by its higher resistance to ductile crack initiation, leading to higher fracture initiation energy.

As soon as brittle fracture appeared, the detrimental effect of bainite drastically reduced the fracture energy of microstructure M. Fig. 12 shows that in contrast with the fracture mechanisms of Charpy impact specimens, NPS specimens tended to enhance differences between transition regions of the two microstructures. From the coarse size (20 µm) of cleavage facets observed on NPS specimens of microstructure M up to warm temperatures, this brittle behavior could be attributed to a higher cleavage-to-ductile transition temperature of bainite in NPS specimens than in Charpy specimens. On the contrary, microstructure P showed good agreement between fracture mechanism transition temperatures obtained with NPS specimens and with Charpy specimens, respectively. This could indicate that quasistatic tests on NPS specimens could be more sensitive than conventional Charpy impact tests to microstructural features that exhibit a lower resistance to brittle cleavage (micro) cracking.

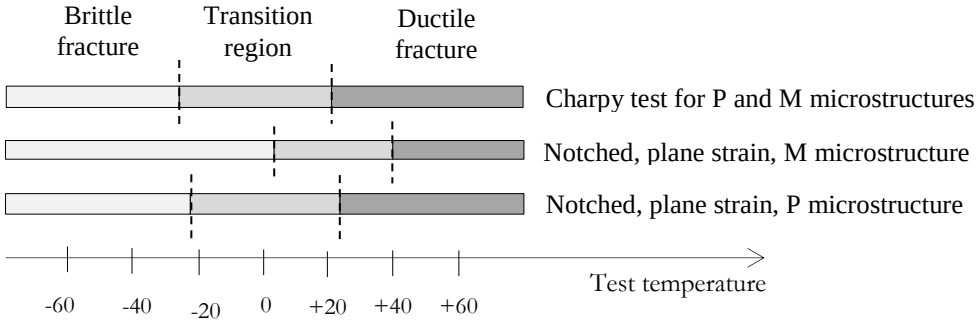

Fig. 12: Comparison of fracture appearance transition behaviors between Charpy impact tests specimens and quasi-static tensile tests on NPS specimens.

4.2. State stress between Charpy and NPS specimens

State stress between Charpy quasi-static and NPS specimens were compare by considering evolution of the three principals stress on the tip of notch, stress triaxiality η and Lode parameter L. All the distributions were calculate along the ligament at the center of Charpy V-notch and NPS (longitudinal direction) specimens. The position x on the ligaments was divided by ω, the distance from

the tip of the notch to the center of the NPS geometries, and near of the bottom for Charpy specimens. This distance is respectively ω = 8mm and ω = 1.5mm for Charpy and NPS geometry. As presented in Fig. 13 (a), the principals stress (S1, S2 and S3) for the two geometries increase and decrease steadily. For the two geometries, S1 stay maximum principal stress while S2 and S3 tend to be the same farther in the tip of notch. Fig. 13 (b) plots evolution of η and L at the tip of the notch. They have same tendency for the two geometries, thus NPS geometry is similar to Charpy V-notch.

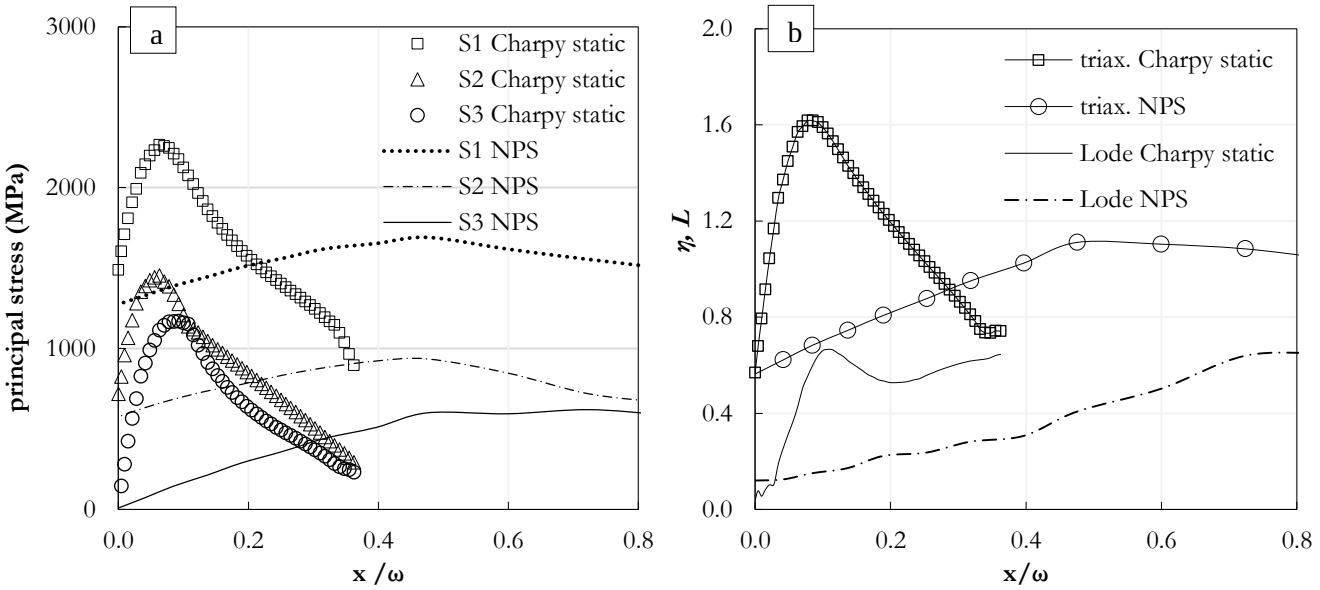

Fig. 13: Comparison of: (a) evolution of principal stress in the tip of notch and (b) state stress between Charpy static and NPS specimen.

5. Conclusion

In the present work, two microstructures P and M taken from a the same bar of a high strength quenched + tempered martensitic steel were study by instrumented Charpy tests and tensile tests on double-side notched plane strain specimens. The mains conclusions are as follows:

1. In both tests, ductile fracture initiated from coarser voids nucleated from inclusions, then from finer voids nucleated from cementite particles; M_2C alloy carbides seem to be too small to initiate fracture during plastic deformation.

2. From Charpy tests, the ductile-to-brittle transition in impact energy was mainly attributed to a transition in propagation energy; nevertheless, the initiation energy steadily increased with temperature, being higher for microstructure M at higher temperature, and lower at lower temperatures. This difference dominated the USE.

3. In addition to the slight effect of finer M_3C carbides, the presence of bainite within the microstructure of steel M tends to contribute significantly to the USE. On the other hand, upper bainite was responsible for the lower resistance of microstructure M to brittle fracture, leading to lower fracture energy in the low-temperature range.

4. Tensile tests on notched plane strain specimens were in qualitative agreement with Charpy results, yet being more sensitive to the cleavage fracture of bainite.

5. Analysis of state stress shows that NPS geometry is in agreement with those of Charpy V-notch specimens.

Acknowledgments

The authors would like to express their gratitude to Franck N'GUYEN for the development of the numerical SKIZ analysis tool, to Gerard BRABANT, Antoine DEBRAY and Kevin BARRIERE for having performed some of the scanning electron microscope analysis. This work is supported by ANRT (French innovation supporting agency) under Grant CIFRE 2016/0670.

References

[1] G. Beranger, G. Henry, G. Labbe, and P Soulignac, *Les aciers spéciaux*, Lavoisier. Paris, 1997.
[2] M. Saby and T. Sourmail, 'Rapport d'avancement sur la connaissance de la trempe-revenu des nuances Oil&Gas', Ascometal CREAS, CREAS R 2014-15, Sep. 2014.
[3] Y. Tomita, 'Low- Temperature improvement of mechanical properties of aisi 4340 steel through high-temperature thermomechanical treatment', *Metall. Trans. A*, vol. 22, no. 5, pp. 1093–1102, May 1991.
[4] S. Takebayashi, K. Ushioda, N. Yoshinaga, and S. Ogata, 'Effect of Carbide Size Distribution on the Impact Toughness of Tempered Martensitic Steels with Two Different Prior Austenite Grain Sizes Evaluated by Instrumented Charpy Test', *Mater. Trans.*, vol. 54, no. 7, pp. 1110–1119, 2013.
[5] Y.-R. Im, Y. Jun Oh, B.-J. Lee, J. Hwa Hong, and H.-C. Lee, 'Effects of carbide precipitation on the strength and Charpy impact properties of low carbon Mn–Ni–Mo bainitic steels', *J. Nucl. Mater.*, vol. 297, no. 2, pp. 138–148, août 2001.
[6] A. Pineau, 'Development of the Local Approach to Fracture over the Past 25 years: Theory and Applications', *Int. J. Fract.*, vol. 138, no. 1–4, pp. 139–166.
[7] L. Xue and T. Wierzbicki, 'Ductile fracture initiation and propagation modeling using damage plasticity theory', *Eng. Fract. Mech.*, vol. 75, no. 11, pp. 3276–3293, juillet 2008.
[8] T. Wierzbicki, Y. Bao, Y.-W. Lee, and Y. Bai, 'Calibration and evaluation of seven fracture models', *Int. J. Mech. Sci.*, vol. 47, no. 4–5, pp. 719–743, avril 2005.
[9] C. Tekoğlu, J. W. Hutchinson, and T. Pardoen, 'On localization and void coalescence as a precursor to ductile fracture', *Philos. Trans. R. Soc. Lond. Math. Phys. Eng. Sci.*, vol. 373, no. 2038, p. 20140121, Mar. 2015.
[10] H. Kim, J. Park, M. Kang, and S. Lee, 'Interpretation of Charpy impact energy characteristics by microstructural evolution of dynamically compressed specimens in three tempered martensitic steels', *Mater. Sci. Eng. A*, vol. 649, pp. 57–67, Jan. 2016.
[11] P. R. Sreenivasan, S. K. Ray, S. L. Mannan, and P. Rodriguez, 'Dynamic fracture toughness and Charpy impact properties of an AISI 403 martensitic stainless steel', *J. Nucl. Mater.*, vol. 228, no. 3, pp. 338–345, avril 1996.
[12] P. Haušild, I. Nedbal, C. Berdin, and C. Prioul, 'The influence of ductile tearing on fracture energy in the ductile-to-brittle transition temperature range', *Mater. Sci. Eng. A*, vol. 335, no. 1–2, pp. 164–174, Sep. 2002.
[13] A. Salemi, A. Abdollah-Zadeh, M. Mirzaei, and H. Assadi, 'A study on fracture properties of multiphase microstructures of a CrMo steel', *Mater. Sci. Eng. A*, vol. 492, no. 1–2, pp. 45–48, Sep. 2008.